OCT-24-2002 09:59 PM P.01

103

Chapter 8

Soft X-ray Absorption Spectroscopy: Applications to Bioinorganic Chemistry

Stephen P. Cramer[1], Hongxin Wang[2], Craig Bryant[2], Mark Legros[2], Craig Horne[2], Daulat Patel[2], Corie Ralston[2], and Xin Wang[2]

[1]Department of Applied Science, University of California, Davis, CA 94306
[2]Structural Biology Division, Lawrence Berkeley National Laboratory, Berkeley, CA 94720

The high brightness of modern synchrotron radiation sources enables a number of x-ray spectroscopic experiments on bioinorganic materials. This review emphasizes developments in biological soft x-ray spectroscopy.

For the past two decades, bioinorganic applications of x-ray spectoscopy have primarily involved structure determination by EXAFS and oxidation state characterization using chemical shifts in the XANES region. Although these have been extremely productive techniques, the purpose of this article is to introduce two less familiar probes - soft x-ray absorption and x-ray magnetic circular dichroism. Bioinorganic applications of these and other x-ray techniques such as high resolution x-ray fluorescence are made possible by the increased brightness of modern synchrotron radiation sources.

X-Ray Transitions. X-ray transitions in atoms involve at least one core level electron. A rather archaic terminology evolved when X-rays were discovered serendipitously by Roentgen more than 100 years ago. Promotion of of a 1s electron is termed K absorption, while K emission involves filling of a 1s vacancy from higher levels. Similarly, L absorption and emission involve 2s or 2p electrons, and so on. L absorption is subdivided into L_3 and L_2 edges, which come respectively from spin-orbit splitting of the $2p^5$ hole into $2p_{3/2}$ and $2p_{1/2}$ final states, and the L_1 edge which results from promotion of the 2s electron. K emission is divided between Kα lines for 2p->1s transitions and Kβ for 3p->1s lines. Finally, Kα1 and Kα2 labels are used to distinguish the spin-orbit splittings of these lines. The many additional intricacies of x-ray nomenclature have been well documented by Agarwal [1].

EXAFS. Extended x-ray absorption fine structure (EXAFS) is a modulation in the absorption cross section past an absorption edge [2]. As illustrated in Figure 1, the final state involves interference between outgoing and backscattered photoelectron waves. Depending on whether this interference is constructive or destructive, there is an enhanced or decreased absorption cross section. As the x-ray energy is changed, the

©1998 American Chemical Society

wavelength of the probe photoelectron changes, and the EXAFS effect periodically alternates in sign. The frequency of this modulation can be used to determine interatomic distances with an accuracy of ± 0.02Å, while the amplitude and phase can be used to extract the numbers and elemental types of neighbors. EXAFS has become an almost routine technique for bioinorganic structure determination, and many fine books and reviews are available [2].

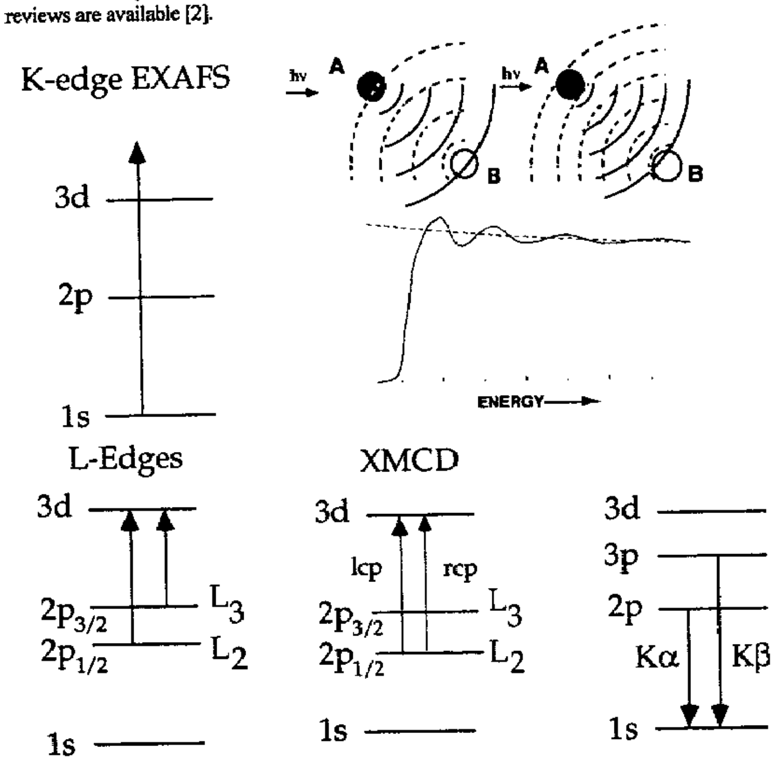

Figure 1. Top panel - (Left) K-edge EXAFS involves a transition from the 1s level to the continuum. (Right) The photoelectron wave from absorber A (——) scatters from neighboring atoms B, and the scattered wave (----) interferes with the original wavefunction to cause the EXAFS effect, as seen in the sample spectrum. Bottom panel - Transitions between discrete levels important for other types of x-ray spectroscopy.

X-Ray Multiplets. When a vacancy is created in a core shell of electrons, the resulting hole can interact with valence electrons to create interesting multiplets. In this way, the core level spectra become sensitive to the valence configuration. Two examples of strong multiplet interactions are first transition metal L-edges, where 2p-3d Coulomb and exchange interactions are important, and Kβ fluorescence, where the 3p-3d exchange interaction dominates (Figure 1).

Synchrotron Radiation

"For revolutions, however we may be tempted to define them, are not mere changes." H. Arendt [3]

The quantitative change in brightness available from synchrotron radiation sources has been so large that it has qualitatively changed the way x-ray science is done. Synchrotron radiation is emitted when relativistic charged particles are deflected by a magnetic field [4]. Because this radiation is highly collimated, synchrotron sources can produce much brighter x-ray beams than available from conventional bremsstrahlung sources (tubes). The first 'generation' of synchrotron radiation sources involved electron storage rings that were primarily used for high energy physics. For these experiments, the electron beams were kept relatively large around most of the ring, and only focussed to a small diameter in the interaction regions. The second generation consisted of sources designed or modified for synchrotron radiation, using mostly bend magnets and wiggler insertion devices. Over the years, machine physicists have learned how to produce extremely low emittance electron beams. This third generation of low emittance x-ray sources that exploits this progress is now coming on line [5, 6]. These rings use 'undulators' with a large number of magnetic poles, designed for constructive interference at certain wavelengths. The resulting radiation is concentrated in space and in frequency. Third generation soft x-ray rings include the ALS in Berkeley [5], ELETTRA in Trieste [7], and the Pohang Light Source in Korea. Undulator beam lines for hard x-rays are available at the ESRF in Grenoble and the APS near Chicago and will soon be available at SPRING-8 in Japan.

Over the past 2 decades, the x-ray brightness available from synchrotron radiation sources has increased by nearly 8 orders of magnitude. This development is frequently called 'revolutionary', and it compares favorably with two better known advances in technology - microprocessors and lasers. X-ray brightness has increased with a doubling time of approximately 12 months (Figure 2). This is comparable to the rate of change in peak power of tabletop lasers, and it is faster than Moore's law for microprocessors.

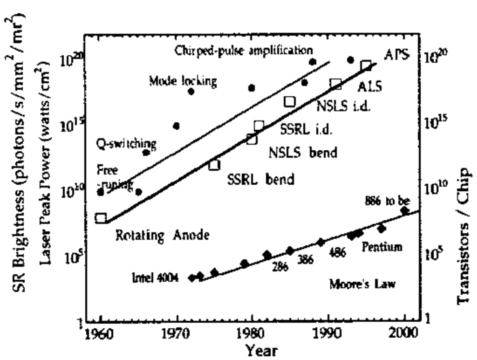

Figure 2. The history of improvement in x-ray brightness from synchrotron sources, compared with other technological revolutions.

Soft X-Ray Absorption

"When I use a word ... it means just what I choose it to mean -- neither more nor less. " - Humpty Dumpty [8]

The term 'soft' for x-rays is used in many ways. For example, in medical technology, 10 keV photons are considered 'soft' x-rays, while in the laser literature, the same label is applied to 0.06 keV photons [9]. For the purposes of this article, we will arbitrarily consider the region from ~100-1100 eV, which includes the K-edges of elements from Be to Na and all of the L-edges from P through Zn. In practical terms, this region is often covered by grazing incidence grating monochromator beamlines at synchrotron radiation labs. Lower photon energies are often covered by higher angle grating beamlines, while at higher energies crystal monochromators take over. Efficient high resolution beamlines for this spectral region were only developed in the early 1980's [10, 11].

Experimental Considerations. Experimental factors make soft x-ray spectroscopy a very different experience from hard x-ray work. Conventional EXAFS measurements can be done in air or helium atmosphere, using moderately thin plastic or Be windows for sample cells, detectors, and cryostats. At many synchrotron radiation labs such as SSRL, NSLS, or the ESRF, a bioinorganic chemist can arrive with a sample and use facility equipment to obtain spectra. In contrast, biological soft x-ray spectroscopy requires a considerable investment in vacuum equipment, primarily because the distance travelled by soft x-rays in aqueous and protein samples is very small.

Absorption Lengths. For example, at the Fe L-edge the 1/e path length for an x-ray in water is only 1.0 micron, and the path length in a helium atmosphere is ~30 cm. This means that any windows used in the apparatus must be extremely thin. One approach is to work in a high vacuum chamber, sometimes in a common vacuum with the beamline and electron storage ring. Setting up the required vacuum conditions often takes days of pumping and 'baking out' a chamber. Small leaks that compromise the vacuum can cost extra days to recover, and if the experimenter makes a mistake that compromises the beamline or ring vacuum, he or she will become instantly famous around the facility.

Detection Methods. Direct measurement of an absorption spectrum involves recording the intensity both with (I) and without (I_0) a sample in place, and then deriving the absorbance (log I_0/I) as a function of x-ray energy (E). However, there are many experimental reasons why it is difficult to record soft x-ray spectra in transmission mode. With concentrated samples such as typical inorganic complexes, the proper thickness to achieve 10% transmission (an absorbance of 1) is on the order of 1000 Å. Since this is much smaller than typical particle sizes, it becomes almost impossible to lay down a homogeneous powder sample with the proper thickness and without significant pinholes and other defects. For dilute samples such as metalloproteins, it is difficult to observe the small changes in transmission at the metal edge on top of the large background signal from water and protein absorption. To avoid artifacts and achieve better sensitivity, 'secondary' detection methods are used (Figure 3). The derivation of these methods and possible artifacts have been extensively reviewed [12].

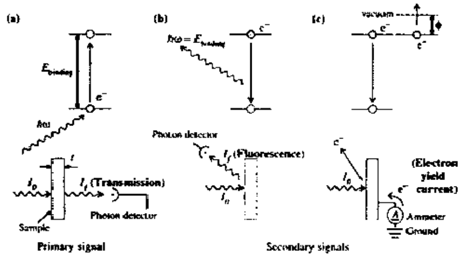

Figure 3. Schematic illustration of different detection modes [49].

In the soft x-ray region, atoms relax after x-ray absorption primarily by emission of an Auger electron. One can measure a signal related to the absorption cross section by recording either the Auger electron yield (I_{auger}/I_0) or the total yield of electrons (I_{tey}/I_0) which are created in a cascade process as the Auger electron energy is dissipated. Auger yield detection requires an electron energy analyzer, and since only a small fraction of these electrons escape from the sample without energy loss, it is relatively inefficient. The most common detection methods are to either measure secondary electrons emerging from the sample (total electron yield) [13] or to measure the electrons passing through the sample (sample photocurrent) with a charge sensitive amplifier (Figure 3).

Since the electron escape depth is short (<100 Å), electron yield techniques are very surface sensitive. Even with excellent glove box or Schlenk techniques, many reactive samples such as Fe-S complexes are coated with a surface oxide that will give unrepresentative and misleading spectra. It is often necessary to sputter or physically scrape samples in vacuum to assure surface integrity. Furthermore, electron yield techniques are not applicable to most metalloproteins. Even if a signal can be observed, it only probes the first protein molecule at the surface of the sample, which may not be representative of the bulk. Furthermore, with total electron yield there is no elemental selectivity and the metal signal will be swamped by the absorption by water and protein background absorption. One is therefore forced to measuring the fluorescence signal (F/I_0) [14], even though L fluorescence yields for transition metals are less than 1%.

Fluorescence detected x-ray absorption is the dominant technique for hard x-ray EXAFS experiments, where its superior sensitivity has long been recognized [15]. The merits and pitfalls of fluorescence detection can be appreciated from the following approximate expression for a 'spectroscopically thick' sample [16]:

$$\frac{F}{I_0} \propto f_s \frac{\mu_s(E)}{\mu_s(E) + \mu_b(E) + \mu_s(E_f) + \mu_b(E_f)} \qquad (1)$$

Here f_s represents the fluorescence yield for the sample element of interest, $\mu_s(E)$ and $\mu_s(E_f)$ are the absorption coefficients for this element at the excitation and fluorescence energies respectively, while $\mu_b(E)$ and $\mu_b(E_f)$ are corresponding coefficients for the background absorption by the matrix. Clearly, if $\mu_s(E)$ is not small compared to $\mu_b(E)$, then the linear relationship between F and $\mu_s(E)$ breaks down. This is properly called fluorescence 'saturation'. The linearity can also break down if the fluorescence and absorption energies of the sample overlap. If E_f changes with excitation energy and $\mu_s(E_f)$ is significant, the amount of escaping fluorescence will vary with E, mimicing a variable fluorescence yield. This is a true 'self-absorption' effect. Both of these problems can be considered 'extrinsic', because they can be solved by making the sample more dilute.

'Intrinsic' artifacts are also possible with fluorescence detection if the fluorescence yield f_s is varies significantly across the absorption spectrum or if different fluorescence lines have different angular distributions, as noted by deGroot [17, 18]. Dramatic differences between electron yield and fluorescence spectra have been observed [19] and explained [20] for Tm^{3+} (Figure 4). However, for the later transition metals, the discrepancy between fluorescence yield and true absorption spectra is predicted to be small [21], and this is also what is experimentally observed (Figure 4).

Table 1. Comparison of Different Detection Modes

Technique	Quantity measured	Probe Depth	Typical Detector
Auger yield	Auger electrons	~20 Å	CMA
Total electron yield	departing electrons	~50-75 Å	channeltron
Sample photocurrent	recharging electrons	~50-75 Å	
Fluorescence	fluorescent x-rays	~50 - 5,000 Å	Ge or Si detector
Transmission	transmitted x-rays	~ 100 - 10,000 Å	PIN diode

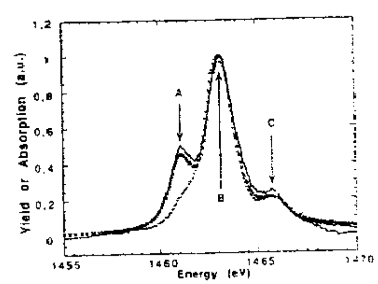

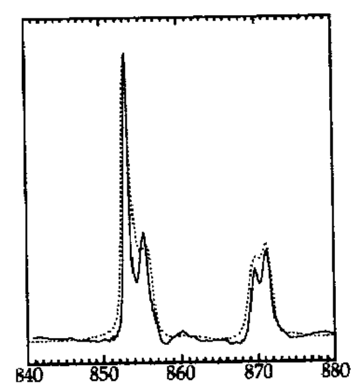

Figure 4. (Left) Transmission (—), electron yield (xxxx) and fluorescence-detected (····) x-ray spectra for Tm_2O_3 [19]. Feature A is almost missing from the fluorescence data(Right) Fluorescence detected absorption for Ni-doped MgO (—) and electron yield for NiF_2 (----). The same features are seen in both spectra.

Radiation Damage. The absorption of x-rays results in ejection of photoelectrons, Auger electrons, and the subsequent production of hydrated electrons and numerous free radicals [22, 23]. Even at low temperatures the electrons can migrate and react with the sample. Because the x-ray path lengths are approximately 3 orders of magnitude shorter than for hard x-rays, while the x-ray energy is only 1 order of magnitude lower, the radiation dose per unit volume is 100 times higher for comparable photon fluxes. Our experience is that proteins with high oxidation potentials are often reduced in the soft x-ray beam (Figure 5). Radiation damage will be an even greater issue in the future when brighter undulator beamlines become available. Crystallographers and microscopists using undulator sources have observed that samples often survive for only a few seconds. However, photoreactivity need not be an insurmountable problem. Because samples only have to be a few microns thick, it should be possible to prepare large sample areas and quickly spin or translate a sample across the photon beam.

What Makes Soft X-Ray Absorption Useful for Bioinorganic Problems? The advantages of the soft x-ray region for inorganic and biological spectroscopy include better energy resolution, favorable selection rules, multiplet splittings and strong magnetic circular dichroism. In the hard x-ray region, transition metal K-edges have linewidths of 1-2 eV, while the intrinsic linewidths of L-levels are much narrower (300-700 meV) [24]. The widths of light element K-edges are even sharper, such that vibrational fine structure can sometimes be seen in gas phase spectra. Better resolution is one factor that makes it easier to distinguish between different oxidation states with L-edges, and it also makes quantitation of mixtures more accurate.

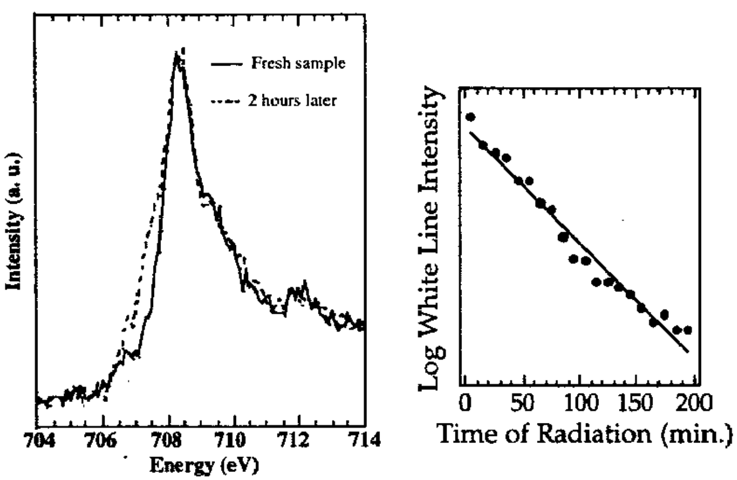

Figure 5. (Left) Mn L-edge spectra of superoxidized *Lactobacillus plantarum* Mn catalase recorded from fresh sample (—) and after 2 hour x-ray exposure (----) [25]. (Right) Time course of the photoreduction of the Cu A site of cytochrome oxidase.

L-edge spectra measure dipole-allowed 2p->3d transitions, while at the K-edge the 1s->3d transition is a weak quadrupole proceess (sometimes enhanced by p-d mixing). Since most of the chemistry of the transition metals involves d-orbitals, L-edges are a natural choice for probing the metal electronic structure. L-edges show multiplet structure that is sensitive to the metal oxidation and spin states, and they also have much larger potential XMCD effects. The net result of these factors is illustrated in Figure 6, where the K and L edges of $MnCl_2$ are compared.

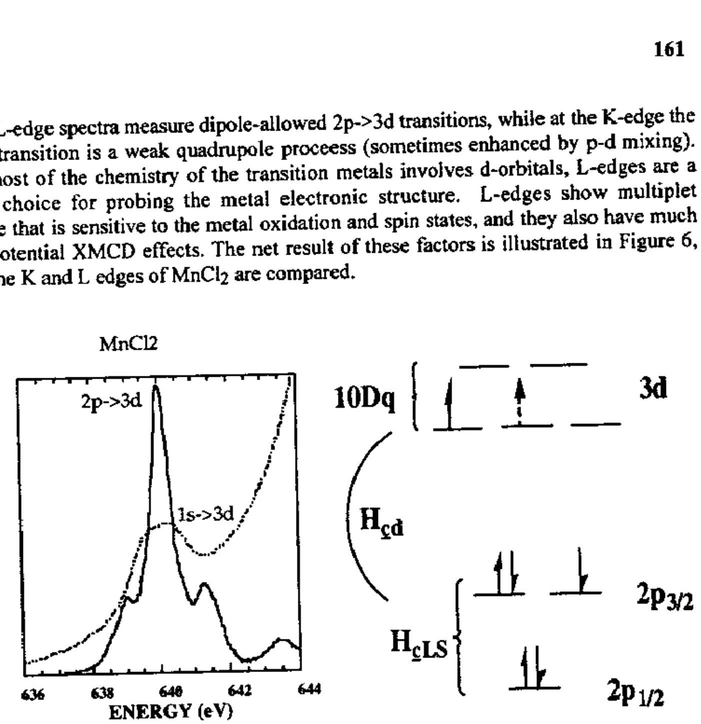

Figure 6. (Left) Comparison of the 1s->3d region of the $MnCl_2$ K-edge with the L_3 edge[26]. (Right) Some of the interactions that give rise to L-edge fine structure.

The Hamiltonian. One way to summarize the factors that affect the position, intensity, and shape of L-edge spectra is to consider the Hamiltonian that describes the initial and final state energies [27]. For inorganic complexes, the most successful procedure for constructing this Hamiltonian is the ligand field multiplet model. Building on ideas developed in the seventies [28, 29], this approach was extensively developed by Thole and coworkers [30], who successfully combined the chain of groups theory of Butler [31] with atomic Hartree-Fock methods from Cowan and coworkers [32]. This method begins by evaluating the atomic multiplets that arise from a given configuration of core hole and valence electrons. Symmetry and ligand field parameters are then used to calculate how these multiplets are split by the ligand environment. In the following examples, we use the notation of deGroot for the relevant Hamiltonians [27].

For example, consider a transition metal ion with N 3d electrons. The L-edge transition can then be described as a $2p^63d^N \rightarrow 2p^53d^{N+1}$ transition. The Hamiltonian for the ground state atomic multiplets is:

$$\mathcal{H}_{1s} + \mathcal{H}_{mu} + \mathcal{H}_{3d} \qquad (2)$$

where $\hat{\mathcal{H}}_{3d}$ is the average energy of the 3d states, $\hat{\mathcal{H}}_{mu}$ includes all 2-electron integrals and $\hat{\mathcal{H}}_{ls}$ is the the 3d spin-orbit coupling. The Hamiltonian for the final state includes extra terms $\hat{\mathcal{H}}_{c}$ for the core hole energy, $\hat{\mathcal{H}}_{c.ls}$ for the core hole spin-orbit splitting, and $\hat{\mathcal{H}}_{c.3d}$ for the core-valence Coulomb and exchange interactions. We consider the effects of terms in this Hamiltonian in reverse order.

$$\hat{\mathcal{H}} = \hat{\mathcal{H}}_{ls} + \hat{\mathcal{H}}_{mu} + \hat{\mathcal{H}}_{c.3d} + \hat{\mathcal{H}}_{3d} + \hat{\mathcal{H}}_{c} + \hat{\mathcal{H}}_{c.ls} \qquad (3)$$

Core Hole Spin-Orbit Splitting. L-edges are split into L_3 and L_2 regions by the spin-orbit interaction of the $2p^5$ core hole - $\hat{\mathcal{H}}_{c.ls}$, which grows stronger with increasing atomic number. Since this splitting is essentially an atomic property, there is probably little chemical information here compared to other features in the spectrum.

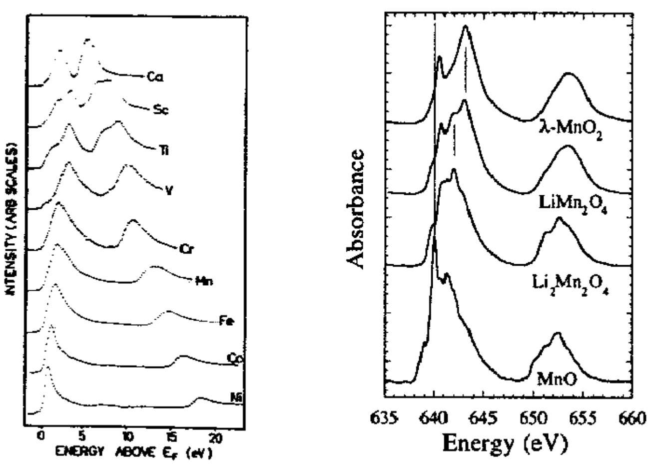

Figure 7. (Left) Changes in spin-orbit splitting in L-edges across the first transition metals. (Right) The shift in L_3 edge position with oxidation state for a series of Mn oxides. $LiMn_2O_4$ is mixed-valence and shows features both Mn(III) and Mn(IV) features.

Chemical Shifts. The chemical shifts of photoelectron energies to higher energy with increasing oxidation state are often explained as a reduction in the screening of the nucleus by valence electrons - hence an increase in the apparent nuclear charge. However, K-edge shifts are complicated by their dependence on interatomic distance [33], and K-edge shifts are too large to be explained as changes in core-level binding energies. In comparison, L-edge shifts are smaller, and some fraction is certainly due to changes in $\hat{\mathcal{H}}_{c}$. Typical chemical shifts for Mn compounds in different oxidation states are illustrated in Figure 7.

Ligand Field Splittings. The influence of the crystal field $\hat{\mathcal{H}}_{3d}$ on L-edges is one of the most important reasons why these spectra are chemically useful. When the splitting of 3d orbital energies is large, its effect can be directly observed in L-edge spectra. For example, a ~4 eV splitting is seen in the L_3 edge of $K_3[Fe(CN)_6]$ (Figure 8). In many other cases $\hat{\mathcal{H}}_{3d}$ is of the same order as other terms in the Hamiltonian, such as $\hat{\mathcal{H}}_{mu}$ and $\hat{\mathcal{H}}_{c.mu}$, and the complete Hamiltonian has to be considered. It can then be misleading to try to read orbital splittings directly from the spectra (Figure 9).

Another way ligand field splittings can affect the spectra is by changing the initial spin state of the complex. Thole and van der Laan have shown that the ratio of L_3 intensity to total intensity (L_3+L_2), the 'branching ratio', [30] changes with spin state. The so-called 'statistical' branching ratio is 4:(4+2) - the ratio of the number of electrons assigned to $2p_{3/2}$ and $2p_{1/2}$ levels respectively. For high spin complexes, there can be substantial deviations from this ratio of 2/3. For example, a typical branching ratio for high-spin Ni(II) complexes is ~0.77[34], and even higher branching ratio are seen for high spin Fe [35] and Mn complexes [26]. In contrast, branching ratios for low spin Ni(II), Fe(II), and Mn(II) complexes are close to the statistical value.

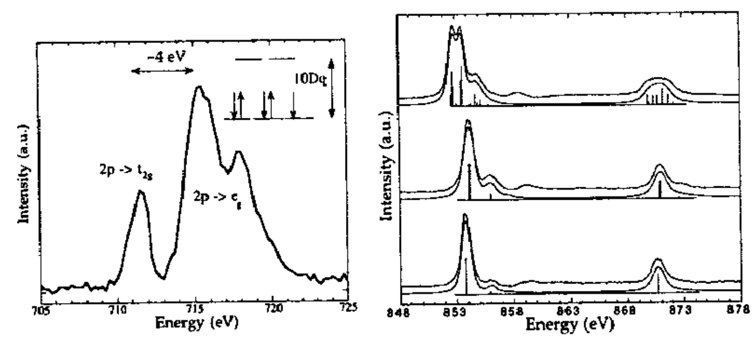

Figure 8. (Left) The L_3 edge for $K_3[Fe(CN)_6]$. (Right) The difference between low-spin and high-spin Ni(II) spectra, illustrated respectively by high spin $[Ni(cyclam)]Cl_2$, low-spin Ni(salen), and low-spin $[Ni(cyclam)](ClO_4)_2$.

Coulomb and Exchange Interactions. For metal complexes with fewer than 9 d electrons, there will be final state vacancies in both the 2p and 3d shells, and the final state will show multiplet structure from 2p-3d interactions - $\hat{\mathcal{H}}_{c.3d}$. For a $3d^N$ transition metal complex, the final state multiplets derive from $2p^5 3d^{N+1}$ configurations with different couplings between 2p and 3d electrons. The simplest case to consider involves complexes which are originally d^0, such as K^+ and Ca^{2+}. Theoretical spectra for d^0 complexes have been calculated and explained in great detail by deGroot and coworkers [36]. They show that for isolated ions, the final state symmetry can be obtained as the product of the ^2P p-hole symmetry and the ^2D d-valence symmetry:

$$2P \otimes {}^2D = {}^1P_1 + {}^1D_2 + {}^1P_3 + {}^3P_{0,1,2} + {}^3D_{0,1,2} + {}^3F_{2,3,4} \qquad (4)$$

In an octahedral ligand field, the spherical SO_3 atomic symmetries are projected to cubic O_h symmetry. The symmetry of the dipole matrix element:

$$< 3d^0 | r | 2p^5 3d^1 > \quad (5)$$

is the product of the symmetries of the initial state (A_1), the dipole operator (T_1) and the final state symmetry, which must also be T_1 for an allowed transition. From the $SO_3 \rightarrow O_h$ branching rules [27, 31], it turns out there are 7 different allowed final states of T_1 symmetry. The relative energies and intensities of the transitions change dramatically with the strength of the crystal field (Figure 9).

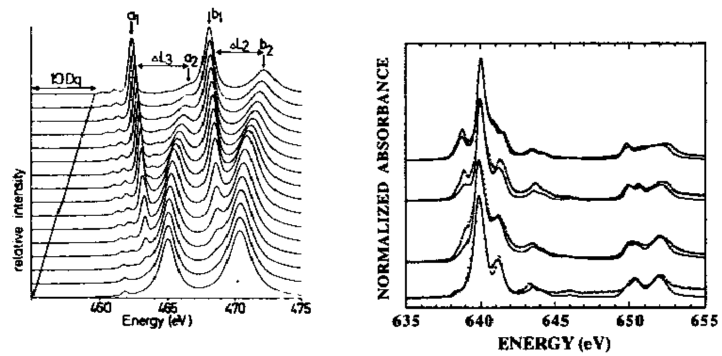

Figure 9. (Left) Calculated L-edges for Ti^{4+} vs. 10Dq, from 0 (bottom) to 4.5 eV (top) [27, 36]. (Right) Experimental spectra (······) and theoretical simulations (—) for a series of Mn complexes [26]. 10Dq increases from -0.3 eV to +1.05 eV from bottom to top.

Relatively simple spectra are also obtained for low spin Ni(II), where the final state now has a single d hole instead of a single d electron. For other cases, the spectra rapidly become too complex for simple explanation - for a $2p^5 d^5$ final state there are 1536 final states! This complexity can nevertheless be handled by the ligand-field multiplet software. Calculations for all of the common transition metals have been published both without [37] and with inclusion of 3d spin-orbit coupling [38].

For completeness, we must mention one last term - $\mathcal{H}_{ls}$ - the 3d spin-orbit coupling. As noted by deGroot [27], this term can be important for the ground state of certain ions with partially filled t_{2g} orbitals, such as $3d^1$, $3d^2$, low-spin $3d^4$, low-spin $3d^5$, high-spin $3d^6$, and high-spin $3d^7$ configurations. Significant changes in the spectrum can occur because of $\mathcal{H}_{ls}$, as shown in Figure 10.

Covalency Effects. The description of L-edge transitions presented so far works well for ionic complexes such as low oxidation state transition metal oxides, fluorides and chlorides. For more covalent compounds, such as higher formal oxidation states or transition metal sulfides, the single configuration model starts to break down.

Experimentally, the multiplet splittings become less pronounced (and less useful), and one is forced to use integrated quantities such as the centroid position and branching ratio.

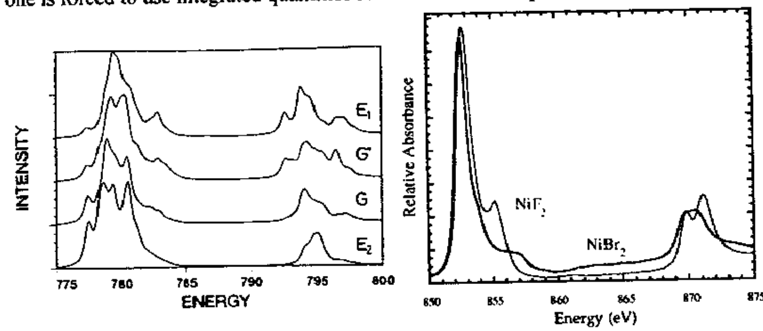

Figure 10. (Left) The effects of 3d spin-orbit coupling on L-edge spectra of cobalt complexes (Right) The loss of multiplet structure in $NiBr_2$ compared to NiF_2.

Covalency can be accomodated in the ligand field multiplet model empirically by reducing the values of the Slater integrals that produce the multiplet terms. A more rigorous procedure is to include configuration interaction in the initial and final state wave functions. The ground state is written as:

$$\Phi_i = \sin\alpha\, [\, 3d^N \,] + \cos\alpha\, [\, 3d^{N+1} \underline{L} \,] \quad (6)$$

while the final state is written as:

$$\Phi_f = \sin\beta\, [\, 2p^5 3d^{N+1} \,] + \cos\beta\, [\, 2p^5 3d^{N+2} \underline{L} \,] \quad (7)$$

If there is a change in the covalency between the intial and final states, then 'satellite' transitions can occur. The relative intensity of the main peak is given by $\cos^2(\beta-\alpha)$ and the satellite intensity is $\sin^2(\beta-\alpha)$ [39]. Satellite features can be seen at about 857-8 eV in following Ni enzyme spectra.

Application to Ni Proteins. NiFe hydrogenases catalyze the oxidation and formation of molecular hydrogen and contain a single Ni site as well as several different Fe-S clusters [40]. The NiFe hydrogenase from *D. gigas* is an $\alpha\beta$ heterodimer containing two Fe_4S_4 clusters, an Fe_3S_4 cluster, and a NiFe center. Crystallographic data on the *D. gigas* enzyme reveals a 5-coordinate Ni site, bridged through sulfur ligands to an unusual Fe species [41] now known to have one CO and two CN^- ligands. There has been considerable debate about whether the EPR signals from hydrogenase represent Ni(I) or Ni(III) [40], and the redox states of the EPR-silent species are also disputed. L-edge spectroscopy can provide complementary information to magnetic resonance, K-edge, infrared, and crystallographic studies of the enzyme.

We have looked at hydrogenase samples from a number of species, including *Pyrococcus furiosus* [42], *Desulfovibrio baculatus*, and *Desulfovibrio desulfuricans* (Figure 11). Although the multiplet structure is suppressed by the covalency of the Ni site, the features of the as-isolated enzyme spectra are best simulated using high spin Ni(II). Previous magnetic susceptibility data had identified the site as diamagnetic [43], and there is always the possibility that the Ni spin state changes under L-edge experimental conditions. We are currently using FT-IR to investigate the characteristic CO and CN stretching frequencies of the NiFe site in partially dried films. The films yield beautiful IR spectra, and the preliminary results show that redox changes seen in frozen solution spectra also appear in the films.

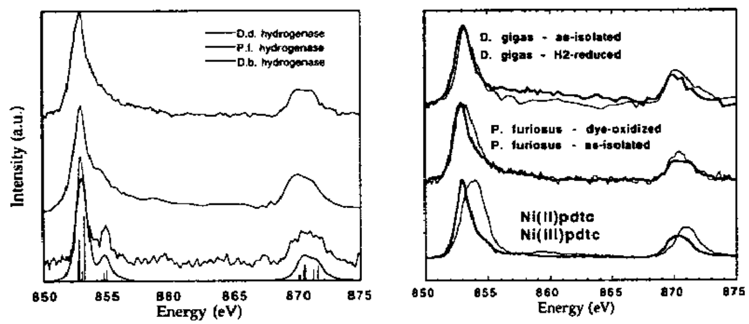

Figure 11. (Left) Ni L-edge spectra for (top to bottom) *P. furiosus* [42], *D. desulfuricans* and *D. baculatus*, as purified, and a high-spin Ni(II) simulation. (Right) Redox shifts in L-edges - (Top to bottom) *D. gigas* as-isolated vs. H_2-reduced, *P. furiosus* oxidized vs. reduced, and $[Ni(II)(pdtc)_2]^{2-}$ vs. $[Ni(III)(pdtc)_2]^{-}$ [42].

L-edge spectroscopy can be used to detect redox activity at the Ni site which is invisible by EPR. For example, the *P. furiosus* enzyme does not show any Ni EPR signals as isolated in the presence of dithionite, nor when oxidized by thionine at 80 C. Nevertheless, the latter sample has a broader L_3 edge and a sharper and more intense L_2 edge. The trend is similar to that seen in the oxidation of the relatively covalent complex $[Ni(II)(pyridine\text{-}2,6\text{-}dithiocarboxylate)_2]^{2-}$ to the monoanion [42]. In the related system $Li_xNi_{1-x}O_2$, these kinds of changes have been interpreted as the mixing of low spin character into the d^8 part of a $d^8\underline{L}$ (ligand hole) ground state. Although the terminology is very different, this is similar to proposals that posit significant charge delocalization in the electronic structure of hydrogenase.

Because there is little structure to the hydrogenase Ni L-edges, we have sought other ways to classify the Ni sites. One approach is to look at the correlation between the L_3 centroid energy and the branching ratio (Figure 12). Most Ni model complexes cluster in discrete regions of such a diagram. We found that H_2- or dithionite-reduced hydrogenases resemble high-spin Ni(II), while CO dehydrogenase has more low-spin Ni(II) character [44]. Oxidized samples of both enzymes resemble covalent Ni(III) species. We have also seen evidence for a Ni(I) component under certain conditions.

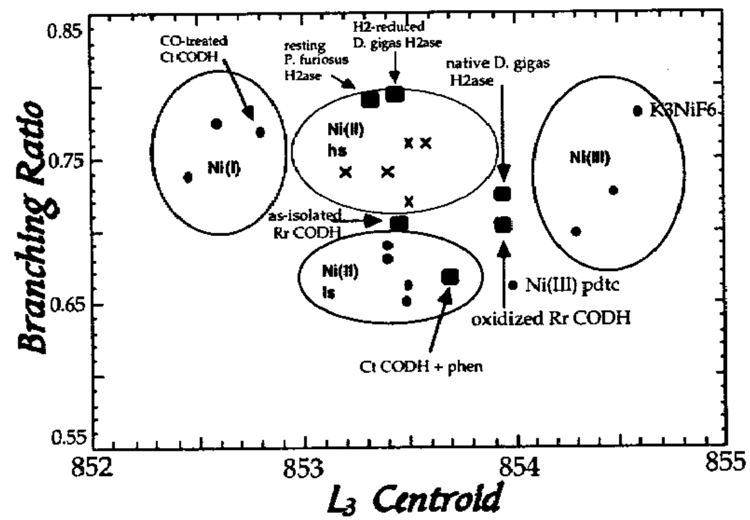

Figure 12. Centroid position and branching ratio for different Ni compounds.

"'Is there any point to which you wish to draw my attention?
'To the curious incident of the dog in the night-time.'
'The dog did nothing in the night-time.'
'That was the curious incident.'
Shirlock Holmes [45]

Integrated Cross Section Sum Rule. Just as the detective inferred a crime from the absence of an event, we can deduce the distribution of electrons in a compound by measuring the presence of 'holes'. The total cross section sum rule for L-edges says that that the intensity integrated over the L_3 and L_2 'white lines' is proportional to the number of empty states. Since the cross sections for 2p->3d transitions are 25 times larger than the 2p->4s cross section [16], one is primarily sensitive to the 3d character of these states. One can therefore measure the metal 3d vacancies by integrating the L-edges.

In practice, absolute cross sections are difficult to measure. This problem is overcome by normalizing the integrated intensity to a region high above the continuum (Figure 13). With the assumption that the continuum cross section is chemically invariant, the normalized spectra can be calibrated by reference to standard compounds with known electronic structure.

Application to Cu Proteins. Blue copper proteins such as plastocyanin are critical for electron transfer in many living systems, and their electronic structure has been studied for decades [46]. Plastocyanin is thus an ideal system for testing different kinds of sum rule analysis, because its electronic structure is well understood from a variety of approaches [46, 47]. The integrated L-edge intensity for plastocyanin was compared with values for $[CuCl_4]^{2-}$ complexes [48], where the electronic structure is well-known. The results are consistent with previous work showing that the half-occupied HOMO is highly covalent with only ~42% Cu $d_{x^2-y^2}$ character (Figure 14).

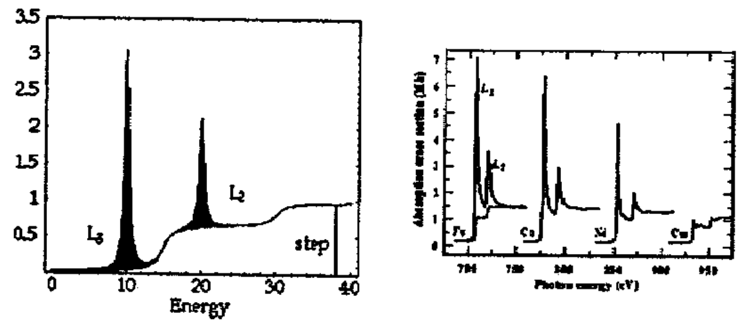

Figure 13. (Left) Schematic illustration of the normalization process. (Right) Normalized L absorption edges for Fe, Co, Ni, and Cu [49].

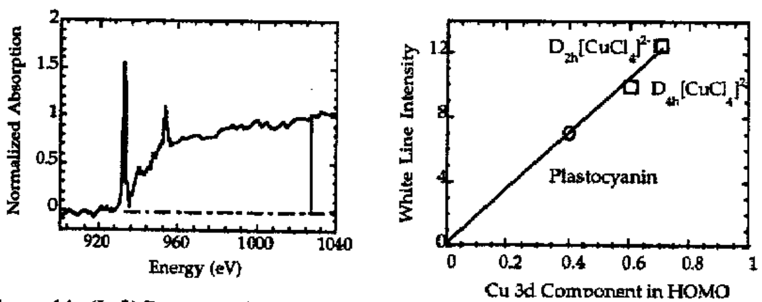

Figure 14. (Left) Representative L-edge spectra for Cu plastocyanin. (Right) Calibration of the Cu white line intensity with respect to $[CuCl_4]^{2-}$ [48].

X-Ray Magnetic Circular Dichroism

X-ray magnetic circular dichroism (XMCD) measurements involve comparing the absorption of left- and right-circularly polarized light by a magnetized sample [50]. XMCD was first observed with hard x-rays in 1987 [51] and with soft x-rays in 1990 [52]. Since then, XMCD has been used to investigate magnetic thin films [53, 54], magnetic alloys [55], and even to image domains on computer disks [56] (Figure 15). Most studies to date have involved ferro- or ferrimagnets, which are easily magnetized near room temperature. Experiments on dilute paramagnetic samples require high fields, low temperatures, and fluorescence detection; this was first accomplished for metal centers in proteins using the Fe in rubredoxin [31].

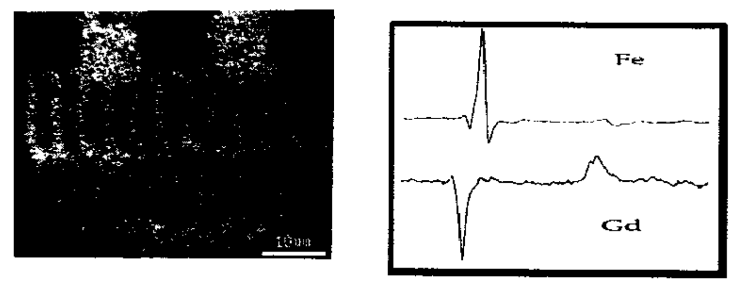

Figure 15. (Left) Photoelectron microscope image of a computer disc test pattern taken by Stöhr and coworkers, wich circularly polarized x-rays [56]. The light and dark regions correspond to magnetic domains polarized in different direction. (Right) The Fe L-edge and Gd M-edge XMCD spectra of $Fe_3Gd_3O_{12}$ reported by Chen *et al.* [55]. The opposite signs show that the Gd and Fe sublattices are antiferromagnetically coupled.

The XMCD effect at *3d* transition metal $L_{2,3}$ edges derives from non-uniform occupation of a Zeeman split initial state, combined with angular momentum rules that determine the intensity of transitions to various final states. Although many transition metal complexes show strong XMCD, the effect is easiest to explain for atomic transitions. For a transition of an atom or ion with angular momentum quantum numbers J and M_J to a new state with quantum numbers J' and $M'_{J'}$, one can use the Wigner-Eckart theorem to separate the matrix element into into radial and angular parts [32]:

$$\langle\phi(J\,M_J)|r_q|\phi(J'\,M'_{J'})\rangle = (-1)^{J-M_J}\begin{pmatrix} J & 1 & J' \\ -M_J & q & M'_J \end{pmatrix}\langle\phi(J)|r_q|\phi(J')\rangle \quad (8)$$

The term in large parentheses is the so-called 3j symbol. For this term to be nonzero, it is necessary that $q=M'_{J'}-M_J$. If we call 'left circularly polarized' x-rays q=1, then the ground state can only have transitions to $M'_{J'}=M_J+1$ with left circular polarization or $M'_{J'}=M_J-1$ with right circular polarization. We remind the reader that there is considerable dyslexia in the definition of left and right circular polarization; our convention is that described by Atkins [57], in which the electric field vector moves like a right handed screw.

A more intuitive explanation for the XMCD effect is illustrated in Figure 16. Here it can be seen that the magnetic moment of the sample is oriented by the applied field. This field also dictates the orientation of the Cu^{2+} spin, hence of the spin of the single hole in the d-shell. Since the electron spin does not change during the electric dipole transition, the spin-orientation of the 2p hole is governed by the original 3d hole orientation. The strong spin-orbit coupling in the 2p shell then dictates the required orbital angular momentum for the 2p hole. Only a q=1 left circularly polarized photon can accomplish the required increase in orbital angular momentum. The important point is that the XMCD effect comes out of conservation of angular momentum.

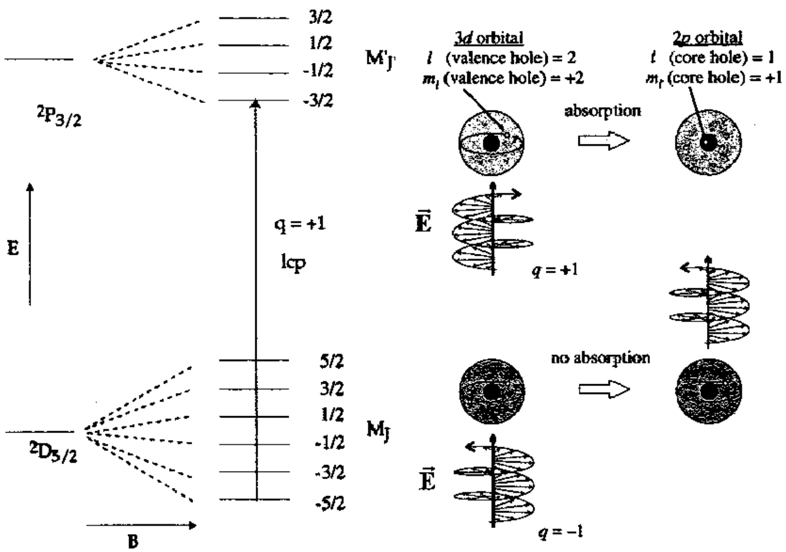

Figure 16. Schematic illustration of the XMCD effect for atomic Cu^{2+}. (Left) The energy levels in a magnetic field, and the allowed transition at 0 K. (Right) An atom interacting with electric field vector of circularly polarized photons [49].

In a ligand field, J is no longer a good quantum number, and the ground state is a mixture of J, M_J wavefunctions. Nevertheless, an XMCD effect is often preserved [58]. The sign of the XMCD effect reveals the local magnetic moment orientation, while the intensities and relative weights can be used to derive spin and orbital moments. Ligand field multiplet programs which calculate L-edges can also simulate metal complex XMCD spectra [59].

Experimental Considerations. The technology for soft x-ray MCD in the transition metal L-edge region differs substantially from UV-visible instrumentation. There are no good quarter wave plate polarizers in this region. Most of the instrument has to be under high vacuum. Transmission experiments are impractical for most metalloproteins. One saving grace is that soft x-ray MCD effects can be quite strong.

Sources of Circular Polarization. One of the simplest ways to obtain circularly polarized synchrotron radiation is to collect the out-of-plane x-rays from bend magnets [60]. As shown in Figure 17, the degree of circular polarization increases rapidly with a small angular excursion from the bending plane, and opposite degrees of

polarization are obtained above and below this plane. However, bend magnet sources are relatively weak, and it is difficult to change from left to right circular polarization without some slight affect on the photon beam energy, spot size or degree of polarization.

A number of insertion device designs provide brighter and more flexible sources of circular polarization, as reviewed by Elleaume [61]. These devices include elliptical wigglers, asymmetric wigglers, crossed undulators, and elliptical undulators. A 75 pole elliptically polarizing undulator is under construction at the Advanced Light Source, and a good fraction of the beamtime will be available for bioinorganic applications.

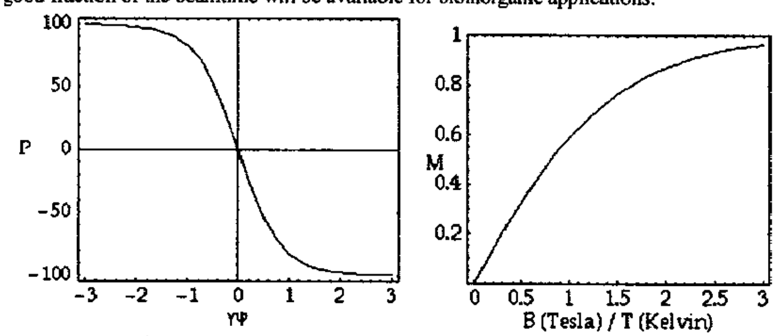

Figure 17. (Left) The degree of circular polarization at 854 eV as a function of off-axis angle φ (in radians) from an SSRL bend magnet. γ is the ratio of the electron energy (3 GeV) to its rest mass energy (0.511MeV). At φψ=1 the angle is approximately 0.01 degrees. (Right) Magnetization curve for a spin 1/2 system.

Field and Temperature. In conventional MCD terminology, XMCD is primarily a 'C term' effect (arising from Zeeman splitting of the ground state) which should have a strong temperature dependence. For a spin 1/2 system, the dependence of the magnetization M on field H and temperature T is given by the Brillouin function [62]:

$$\frac{M}{M_0} = \tanh\left(\frac{g\, J\, \mu_B H}{kT}\right) \tag{9}$$

where μ_B is the Bohr magneton and k is Boltzmann's constant. What this means in practice is that for ~90% magnetization of dilute paramagnetic systems, a B(Tesla)/T(Kelvin) ratio of ~2 is needed (Figure 18). Our approach has been to use a superconducting split-coil magnet system to provide a magnetic field up to 2 Tesla and a dilution refrigerator to keep the sample below 0.5 K (Figure 18).

What Makes X-Ray MCD Useful for Bioinorganic Problems?. X-ray MCD can provide information that is difficult or impossible to obtain by other techniques. The information content and strengths include (1) elemental selectivity - one can examine one particular element at a time, (2) oxidation state selectivity - it is often possible to resolve the XMCD contributions from different chemical species, (3) direct spin orientations - the sign of the XMCD signal can be used to infer the orientation of a particular magnetic moment, (4) magnetization curves - the B and T dependence of the XMCD can be used to infer spin states, and (5) sum rules - the integrated XMCD signal can be used to deduce the metal-centered orbital and spin moments.

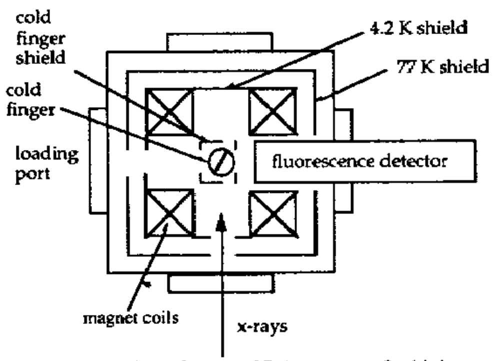

Figure 18. The components of a soft-ray MCD instrument for bioinorganic experiments.

L and S Sum Rules. For 3d transition metal L-edges, the orbital and spin sum rules relate integrated XMCD intensities to element specific projections of the 3d orbital angular momentum $<L_z>$, the 3d spin angular momentum $<S_z>$ and a magnetic dipole term $<T_z>$, as summarized in Equations (10) and (11) respectively. Stöhr and König have shown that the $<Tz>$ term angular averages to zero in 'powder' samples, so this term has been omitted from our equations.

$$\frac{\langle L_z \rangle}{n_h} = \frac{4\int_{L_2+L_3} [A^+(\omega) - A^-(\omega)]\, d\omega}{3\int_{L_2+L_3} [A^+(\omega) + A^-(\omega)]\, d\omega} = \frac{2(A+B)}{3C} \tag{10}$$

$$\frac{\langle S_z \rangle}{n_h} = \frac{\left(\int_{L_3} [A^+(\omega) - A^-(\omega)]\, d\omega - 2\int_{L_2} [A^+(\omega) - A^-(\omega)]\, d\omega\right)}{\int_{L_2+L_3} [A^+(\omega) + A^-(\omega)]\, d\omega} = \frac{(A-2B)}{2C} \tag{11}$$

Here n_h represents the number of 3d vacancies in the metal ion and ω is the x-ray frequency. It is common in the XMCD literature to refer to the first integral in the numerator of (10) as 'A', the second integral as 'B', and the average integrated intensity as C. (Figure 19).

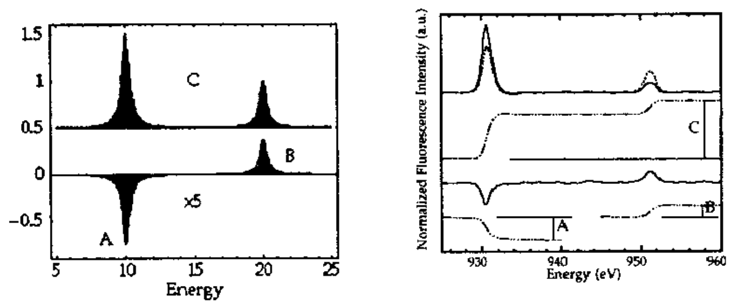

Figure 19. (Left) The integrated quantities important for sum rule analysis. (Right) XMCD spectrum for Cu(II) plastocyanin, along with integrations for sum rule analysis.

Application to Cu Plastocyanin. The XMCD of Cu in oxidized plastocyanin has been used as a test case for sum rule analysis of metalloproteins. After normalizing the overall Cu L-edge jump between 920 and 1050 eV to unity, average numerical values for $A = -3.08 \pm 0.3$, $B = 1.35 \pm 0.2$ and $C = 7.27 \pm 0.3$ were obtained, where the errors refer to the degree of experimental reproducibility. From equation (10), $\langle L_Z \rangle$ is found to be 0.07 ± 0.02 /Cu atom, while from equation (11) we derive 0.18 ± 0.02 /Cu atom for $\langle S_Z \rangle$, all in units of $h/2\pi$. The orbital momentum compares favorably with values using covalent wavefunctions from a converged SCF-Xα-SW calculation, which yield a Cu 3d specific, orientation averaged $\langle L_Z \rangle$ value of 0.059 /Cu atom. The SCF-X-SW calculated $\langle S_Z \rangle$ is 0.21 is also not far from the sum rule values of $\langle S_Z \rangle$. XMCD appears to have promise for providing detailed information about electronic structure that is difficult to obtain by other methods.

Prospects for the Future

"... revolution as we know it in the modern age has always been concerned with both liberation and freedom." Hannah Arendt[3]

The revolution in synchrotron radiation sources has opened the entire realm of x-ray spectroscopy for bioinorganic chemistry. This rapid improvement in technology shows no sign of abating. Plans are already being made for a still brighter fourth generation of synchrotron radiation sources [63]. based on 'free electron lasers' [64]. Cryogenic detectors with exquisite energy resolution are being developed [65]; these devices will eventually allow much more dilute samples to be examined. New capillary x-ray optics [66], x-ray lenses, and x-ray quarter wave plates [67] will enhance our ability to collect and control high energy photons. With more photons and better detectors, other experiments including x-ray Raman [68] and resonance Raman [69] spectroscopy, x-ray emission dichroism [70, 71], and site-selective EXAFS [72] will become feasible on bioinorganic samples.

Over the past two decades, EXAFS spectroscopy has become a routine tool for structure determination. But although this application is more than 20 years old, in many respects we are just beginning to exploit the potential of x-rays for bioinorganic studies. As more and more molecular structures are conquered by the crystallographers, questions remain that cannot be answered by EXAFS or diffraction. When chemists ask in detail - where are the electrons, where are the spins, and how are they coupled - these are questions that can be addressed by x-ray spectroscopy. The number of photons available is no longer the main issue; we are only limited by our own ingenuity.

Acknowledgements

We thank C. T. Chen, F. Sette, G. Sawatzky, S. George, J. van Elp, and F. deGroot for nurturing the early development of bioinorganic soft x-ray spectroscopy. The staffs of the ALS, NSLS, and SSRL also helped make this work possible. This research was supported by the National Institutes of Health (GM-44380), the National Science Foundation (BIR-9317942 and BIR-9105323) , and by the Department of Energy, Office of Biological and Environmental Research. The Stanford Synchrotron Radiation Laboratory is supported by the Department of Energy, Office of Basic Energy Sciences. SPC would also like to ackowledge the memory of Prof. John Fuggle, who helped introduce him to this field.

References Cited

[1.] Agarwal, B. K. (1991) X-ray Spectroscopy : An Introduction, Springer-Verlag, New York.

[2.] Koningsberger, D. C., Prins, R. and eds. (1988) X-ray Absorption : Principles, Applications, Techniques of EXAFS, SEXAFS, and XANES, Wiley, New York.

[3.] Arendt, H. (1963) On Revolution, Viking Press, New York.

[4.] Margaritondo, G. (1988) Introduction to Synchrotron Radiation, Oxford University Press, New York.

[5.] Schlacter, A. S. (1994) in New Directions in Research with Third-Generation Soft X-Ray Synchrotron Light Sources (Schlacter, A. S. and Wuilleumier, F. J., eds.), pp. 1-22, Kluwer Academic Publishers, Dordrecht.

[6.] Hellemans, A. (1997) in Physics Today, vol. 277, pp. 1214-1215.

[7.] "Ultrabright synchrotron source ELETTRA: First period of operation", Margaritondo, G., Savoia, A., Bernstoff, S., Bertolo, M., Comelli, G., DeBona, F., Jark, W., Kiskinova, M., Paolucci, G., Prince, K., Santaniello, A., Tromba, G., Walker, R. and Rosei, R., *Acta Physica Polonica A*, **91**, 631-640 (1997).

[8.] Carroll, L. (1872) Through the Looking Glass.

[9.] "Efficient, high-brightness soft-x-ray laser at 21.2 nm", Rus, B., Carillon, A., Dhez, P., Jaegle, P., Jamelot, G., Klisnick, A., Nantel, M. and Zeitoun, P., *Phys. Rev. A*, **55**, 3858-3873 (1997).

[10.] "Performance of the Dragon Soft X-Ray Beamline", Chen, C. T. and Sette, F., *Rev. Sci. Inst.*, **60**, 1616-1621 (1989).

[11.] "A General Purpose Sub-Kev X-Ray Facility at the Stanford-Synchrotron-Radiation-Laboratory", Tirsell, K. G. and Karpenko, V. P., *Nucl. Inst. Meth. A*, **291**, 511-517 (1990).

[12.] "On Experimental Attentuation Factors of the Amplitude of EXAFS Oscillations in Absorption, Reflectivity, and Luminescence Measurements", Goulon, J., Goulon-Ginet, C., Cortes, R. and Dubois, J. M., *Journal de Physique*, **43**, 539-548 (1982).

[13.] "Probing Depth of Soft X-Ray Absorption Spectroscopy Measured in Total-Electron-Yield Mode", Abbate, M., Goedkoop, J. B., deGroot, F. M. F., Grioni, M., Fuggle, J. C., Hofmann, S., Petersen, H. and Sacchi, M., *Surface and Interface Analysis*, **18**, 65-69 (1992).

[14.] "Soft X-Ray Spectroscopy of Metalloproteins Using Fluorescence Detection", Cramer, S. P., Chen, J., George, S. J., van Elp, J., Moore, J., Tench, O., Colaresi, J., Yocum, M., Mullins, O. C. and Chen, C. T., *Nucl. Inst. Meth. A*, **319**, 285-289 (1992).

[15.] Jaclevic, J., Kirby, J. A., Klein, M. P., Robertson, A. S., Brown, G. S. and Eisenberger, P., *Sol. State Comm.*, **23**, 679 (1977).

[16.] Stern, E. A. and Heald, S. M. (1983) in Handbook on Synchrotron Radiation, vol. 1B (Koch, E., ed.), pp. 955-1014, North Holland, Amsterdam.

[17.] "Fluorescence Yield Detection - Why It Does Not Measure the X-Ray Absorption Cross Section", deGroot, F. M. F., Arrio, M.-A., Sainctavit, P., Cartier, C. and Chen, C. T., *Sol. State Comm.*, **92**, 991-995 (1994).

[18.] "Distortions of X-Ray absorption spectra measured with fluorescence yield", deGroot, F. M. F., Arrio, M.-A., Sainctavit, P., C., C. and Chen, C. T., *Physica B*, **208-209**, 84-86 (1995).

[19.] "Experimental and Theoretical Comparison Between Absorption, Total Electron Yield, and Fluorescence Spectra of Rare-earth M-5 Edges", Pompa, M., Flank, A. M., Lagarde, P., Rife, J. C., Stekhin, I., Nakazawa, M., Ogasawara, H. and Kotani, A., *Phys. Rev. B*, **56**, 2267-2272 (1997).

[20.] "Theory of Fluorescence Yield Spectra of Rare Earth Oxides at 3d Threshold Region", Nakazazwa, M., Ogasawara, H., Kotani, A. and Lagarde, P., *J. Phys. Soc. Jap.*, in press (1997).

[21.] "Polarized X-Ray Fluorescence as a Probe of Ground State Properties", van Veenendaal, M., M. Goedkoop, J. B. and Thole, B. T., *Phys. Rev. Lett.*, **77**, 1508-1511 (1996).

[22.] "On Radiation Damage to Normal Tissues and Its Treatment .1. Growth Factors.", Michalowski, A., *Acta Oncologica*, **29**, 1017-1023 (1990).

[23.] "DNA Damage and Repair Following Treatment with Ionizing Radiation", Powell, S. and Mcmillan, T. J., *Radiotherapy and Oncology*, **19**, 95-108 (1990).

[24.] "Natural Widths of Atomic K and L Levels, Kα X-Ray Lines and Several KLL Auger Lines", Krause, M. O. and Oliver, J. H., *J. Chem. Phys. Ref. Data*, **8**, 329-337 (1979).

[25.] "Manganese L-Edge X-Ray Absorption Spectroscopy of *Lactobacillus plantarum* Catalase and Mixed Valence Manganese Complexes", Grush, M. M., Chen, J., Stemmler, T. L., George, S. J., Penner-Hahn, J. E., Christou, G. and Cramer, S. P., *J. Am. Chem. Soc.*, **118**, 65-69 (1996).

[26.] "Ligand Field Strengths and Oxidation States from Manganese L-Edge Spectroscopy", Cramer, S. P., Degroot, F. M. F., Ma, Y., Chen, C. T., Sette, F., Kipke,

C. A., Eichhorn, D. M., Chan, M. K., Armstrong, W. H., Libby, E., Christou, G., Brooker, S., Mckee, V., Mullins, O. C. and Fuggle, J. C., *J. Am. Chem. Soc.*, **113**, 7937-7940 (1991).

[27.] "X-Ray Absorption and Dichroism of Transition Metals and their Compounds", deGroot, F. M. F., *J. Electron Spec. Rel. Phen.*, **67**, 529-622 (1994).

[28.] "Calculation of Multiplet Structure of Core p-vacancy Levels. II", Gupta, R. P. and Sen, S. K., *Phys. Rev. B*, **12**, 15-19 (1975).

[29.] Asada, S., Satako, C. and Sugano, S., *J. Phys. Soc. Jap.*, **37**, 855 (1975).

[30.] Thole, B. T., van der Laan, G. and Butler, P. H., *Chem. Phys. Lett.*, **149**, 295 (1988).

[31.] Butler, P. H. (1981) Point Group Symmetry Applications, Methods and Tables, Plenum, New York.

[32.] Cowan, R. D. (1981) The Theory of Atomic Structure and Spectra, University of California Press, Berkeley.

[33.] "Bond Distance Determination From X-Ray Absorption Near Edge Structure", Mahto, P. and Chetal, A. R., *Physica B*, **158**, 415-416 (1989).

[34.] "Bioinorganic Applications of X-ray Multiplets - The Impact of Theo Thole's Work", Cramer, S. P., Ralston, C. Y., Wang, H. X. and Bryant, C., *J. Electron Spec. Rel. Phen.*, **86**, 175-183 (1997).

[35.] "Iron L-edge X-ray absorption Spectroscopy of Myoglobin Complexes and Photolysis Products", Wang, H. X., Peng, G., Miller, L. M., Scheuring, E. M., George, S. J., Chance, M. R. and Cramer, S. P., *J. Am. Chem. Soc.*, **119**, 4921-4928 (1997).

[36.] "$L_{2,3}$ X-Ray Absorption Edges of d^0 Compounds - K^+, Ca^{2+}, Sc^{3+} and Ti^{4+} in O_h (Octahedral) Symmetry", deGroot, F. M. F., Fuggle, J. C., Thole, B. T. and Sawatzky, G. A., *Phys. Rev. B*, **41**, 928-937 (1990).

[37.] "2p X-Ray Absorption of 3d Transition Metal Compounds - An Atomic Multiplet Description Including the Crystal Field", deGroot, F. M. F., Fuggle, J. C., Thole, B. T. and Sawatzky, G. A., *Phys. Rev. B*, **42**, 5459-5468 (1990).

[38.] "The 2p Absorption Spectra of 3d Transition Metal Compounds in Tetrahedral and Octahedral Symmetry", van der Laan, G. and Kirkman, I. W., *J. Phys. - Condensed Matter*, **4**, 4189-4204 (1992).

[39.] "Complementary Roles of Co 2p X-Ray Absorption and Photoemission Spectra in CoO", Okada, K. and Kotani, A., *J. Phys. Soc. Jap.*, **61**, 449-453 (1992).

[40.] "Nickel Hydrogenases - In Search of the Active Site", Albracht, S. P. J., *Biochim. Biophys. Acta*, **1188**, 167-204 (1994).

[41.] "Crystal Structure of the Nickel-Iron Hydrogenase from *Desulfovibrio gigas*", Volbeda, A., H., C. M., Piras, C., C., H. E. and etal., *Nature*, **373**, 580-587 (1995).

[42.] "Nickel L-Edge X-ray Absorption Spectroscopy of *Pyrococcus furiosus* Hydrogenase", van Elp, J., Peng, G., Zhou, Z. H., Adams, M. W. W., Baidya, N., Mascharak, P. K. and Cramer, S. P., *Inorg. Chem.*, **34**, 2501-2504 (1995).

[43.] "The Nickel Site in Active *Desulfovibrio baculatus* [NiFeSe] Hydrogenase is Diamagnetic - Multifield Saturation Magnetization Measurement of the Spin State of Ni(II)", Wang, C. P., Franco, R., Moura, J. J. G., Moura, I. and et al., *J. Biol. Chem.*, **267**, 7378-7380 (1992).

[44.] Ralston, C. Y. (1997), Ph. D. Thesis, University of California, Davis.

[45.] Doyle, S. A. C. (1892) The Silver Blaze.

[46.] "Electronic Structure of the Oxidized and Reduced Blue Copper Sites - Contributions to the Electron Transfer Pathway, Reduction Potential, and Geometry", Solomon, E. I., Penfield, K. W., Gewirth, A. A., Lowery, M. D., Shadle, S. E., Guckert, J. A. and Lacroix, L. B., *Inorg. Chim. Acta*, **243**, 67-78 (1996).

[47.] "Structural and Functional Aspects of Metal Sites in Biology", Holm, R. H., Kennepohl, P. and Solomon, E. I., *Chem. Rev.*, **96**, 2239-2314 (1996).

[48.] "Copper L-Edge Spectral Studies - A Direct Experimental Probe of the Ground-State Covalency in the Blue Copper Site in Plastocyanin", George, S. J., Lowery, M. D., Solomon, E. I. and Cramer, S. P., *J. Am. Chem. Soc.*, **115**, 2968-2969 (1993).

[49.] Nakajima, R. (1997), Ph. D. Thesis, Stanford University.

[50.] "X-ray Magnetic Circular Dichroism Spectroscopy of Transition Metal Thin Films", Stöhr, J., *J. Electron Spec. Rel. Phen.*, **75**, 253-272 (1995).

[51.] "Absorption of Circularly Polarized X Rays in Iron", Schütz, G., Wagner, W., Wilhelm, W., Kienle, P., Zeller, R., Frahm, R. and Materlik, G., *Phys. Rev. Lett.*, **58**, 737 (1987).

[52.] "Soft X-Ray Magnetic Circular Dichroism of the $L_{2,3}$ Edges of Nickel", Chen, C. T., Sette, F., Ma, Y.-J. and Modesti, S., *Phys. Rev. B*, **42**, 7262-7265 (1990).

[53.] "Giant X-Ray Absorption Circular Dichroism In Magnetic Ultrathin Films Of Fe/Cu(001)", Tobin, J. G., Waddill, G. D. and Pappas, D. P., *Phys. Rev. Lett.*, **68**, 3642-3645 (1992).

[54.] "Magnetic X-Ray Dichroism in the Spectroscopy of Ultrathin Magnetic Alloy Films", Tobin, J. G., Goodman, K. W., Mankey, G. J., Willis, R. F. and et al., *J. Vac. Sci. Tech. B*, **14**, 3171-3175 (1996).

[55.] "Magnetic Moments in a Gadolinium Iron Garnet Studied by Soft-X-Ray Magnetic Circular Dichroism", Rudolf, P., Sette, F., Tjeng, L. H., Meigs, G. and Chen, C. T., *J. Mag. Mag. Mat.*, **109**, 109-112 (1992).

[56.] "Element-Specific Magnetic Microscopy With Circularly Polarized X-Rays", Stöhr, J., Wu, Y., Hermsmeier, B. D., Samant, M. G., Harp, G. R., Koranda, S., Dunham, D. and Tonner, B. P., *Science*, **259**, 658-661 (1993).

[57.] Atkins, P. W. (1974) Quanta - A Handbook of Concepts, Oxford University Press, Oxford.

[58.] "Magnetic Dichroism in the X-Ray-Absorption Branching Ratio", van der Laan, G. and Thole, B. T., *Phys. Rev. B*, **42**, 6670-6674 (1990).

[59.] "Strong Magnetic X-Ray Dichroism in 2p Absorption Spectra of 3d Transition-Metal Ions", van der Laan, G. and Thole, B. T., *Phys. Rev. B*, **43**, 13401-13411 (1991).

[60.] "Double-Headed Dragon Monochromator for Soft X-Ray Circular Dichroism Studies", Chen, C. T., Sette, F. and Smith, N. V., *Applied Optics*, **29**, 4535-4536 (1990).

[61.] "Insertion Devices For The New Generation Of Synchrotron Sources - A Review", Elleaume, P., *Rev. Sci. Inst.*, **63**, 321-326 (1992).

[62.] Cullity, B. D. (1972) Introduction to Magnetic Materials, Addison-Wesley, Reading, Mass.

[63.] "From the third to the fourth generation of synchrotron radiation light sources", Laclare, J. L., *Journal de Physique*, **7**, 39-46 (1997).

[64.] "Free-Electron Laser Simulation Techniques", Tran, T. M. and Wurtele, J. S., *Phys. Reports*, **195**, 1-21 (1990).

[65.] "High-resolution Superconducting X-ray Spectrometers with an Active Area of 282 µm x 282 µm", Mears, C. A., Labov, S. E., Frank, M., Netel, H., Hiller, L. J., Lindeman, M. A., Chow, D. and Barfknecht, A. T., *IEEE Transactions on Applied Superconductivity*, 7, 3415-3418 (1997).

[66.] "The Use of X-Ray Capillary Optics for Lithography and Microscopy", Arkadiev, V. A., Gorny, H. E., Gruev, D. I., Karnaukhov, A. A., Kolomiitsev, A. I., Kumakhov, M. A., Langhoff, N., Shandintsev, D. V. and Wedell, R., *Optical and Quantum Electronics*, **28**, 309-314 (1996).

[67.] "Perfect Crystal and Mosaic Crystal Quarter-Wave Plates for Circular Magnetic X-Ray Dichroism Experiment", Giles, C., Malgrange, C., Goulon, J., Debergevin, F., Vettier, C., Fontaine, A., Dartyge, E., Pizzini, S., Baudelet, F. and Freund, A., *Rev. Sci. Inst.*, **66**, 1549-1553 (1995).

[68.] "X-ray Raman Spectra from Low-Z Elements", Udagawa, Y., Watanabe, N. and Hayashi, H., *Journal de Physique*, 7, 347-352 (1997).

[69.] "High Resolution X-Ray Resonant Raman Scattering", Carra, P., Fabrizio, M. and Thole, B. T., *Phys. Rev. Lett.*, **74**, 3700-3703 (1995).

[70.] "Dichroism and Spin Information in Soft X-ray Emission", Eisebitt, S., Luning, J., Rubensson, J. E., Schmitz, D., Blugel, S. and Eberhardt, W., *Sol. State Comm.*, **104**, 173-177 (1997).

[71.] "Theoretical Analysis of the Magnetic Circular Dichroism in the 2p3d and 2p4d x-ray emission of Gd", deGroot, F. M. F., Nakazawa, M., Kotani, A., Krisch, M. H. and Sette, F., *Phys. Rev. B*, **56**, 7285-7292 (1997).

[72.] "Site-Selective XANES and EXAFS - A Demonstration With Manganese Mixtures and Mixed-Valence Complexes", Grush, M. M., Christou, G., Hamalainen, K. and Cramer., S. P., *J. Am. Chem. Soc.*, **117**, 5895-5896 (1995).

Reprinted from Symposium Series 692
Spectroscopic Methods in Bioinorganic Chemistry
Edward I. Solomon and Keith O. Hodgson, Editors
Published 1998 by the American Chemical Society